Nano Research

Open Access

Research Article

TiO_2-supported Ni_4 quadruple-atom catalyst: A promising few-atom catalyst with high atomic utilization

Furui Chen, Guangce Zhao, and Gang Zhou

School of Science, Hubei University of Technology, Wuhan 430068, China

Cite this article: *Nano Research*, **2025**, *18*, 94907293. https://doi.org/10.26599/NR.2025.94907293

ABSTRACT: Using density functional theory calculations, we investigate the growth habit and structural stability of Ni_4 tetramer on TiO_2 (Ni_4/TiO_2), which acts as a representative of oxide-supported few-atom catalysts (FACs) ideally with high atomic utilization. We further analyze the structural characteristics and valence state distribution of metals of two structurally different Ni_4/TiO_2 for comparative study in catalysis, typically as hydrogen-related applications. The planar rhombic and tetrahedral Ni_4/TiO_2 feature the coordination environment of central metal atoms and the interfacial bonding from support interactions, respectively. Both structure-dependent binding characteristics and metal valence state distributions determine the active sites, catalytic activity, and reaction pathways and mechanisms in hydrogen production of the two catalysts. The planar rhombic structure exhibits high atomic utilization and outstanding catalytic activity, far exceeding those of the tetrahedral structure in this reaction. According to the atomic utilization and structure-dependent catalytic performance, we define and conceptualize the rising FACs, independent of cluster catalysts. These findings have implications for the design of suitable FACs and the creation of favorable conditions for multi-step reactions.

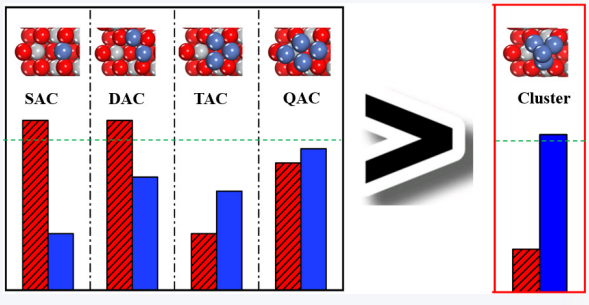

KEYWORDS: few-atom catalysts, quadruple-atom, atomic utilization, density functional theory, hydrogen production, TiO_2-supported Ni_4

1 Introduction

In the past two decades, upholding the classical idea that the smaller the size of supported nanoparticles, the more low-coordinated metal atoms, and the higher the specific activity of each metal atom, scientists have made great efforts to develop atomically dispersed metal catalysts (ADMCs), typically containing single-atom catalysts (SACs) [1–3] and atomically dispersed clusters with a few atoms [4–6]. So far, SACs have revolutionized the field of catalysis like a whirlwind and achieved many achievements in heterogeneous and electrochemical catalysis, with the advantages of high atomic utilization, outstanding catalytic activity and selectivity toward diverse reactions [7]. These advantages are derived from single active centers with the atomic dispersion nature and low atomic coordination number. However, things have changed for atomically dispersed clusters, offering multiple active sites composed of multiple metal atoms [8–10]. That is to say, some advantages from a single active center (nearly 100% atomic utilization) will be lost, and meanwhile, new competitive advantages from the effect of multiple atoms will be created. The most obvious thing is, of course, the uncertainty in identifying and counting active sites available for the reaction. This will lead to the variability of reactions among multiple sites, and the diversity of reaction pathways and products with external conditions. Conversely, these advantages can improve the selectivity and controllability of complex multi-step reactions.

Especially, over the last few years, with the emergence of double-atom catalysts (DACs) [11–13] and triple-atom catalysts (TACs) [14, 15], the concept of few-atom catalysts (FACs) characterized by the number of supported atoms in a close-packed arrangement has gradually entered people's field of vision [5, 16]. Significantly, the FAC concept could visually and quantitatively distinguish between the constituent atoms and active sites in a given region, and then establish a close connection between the two during the reaction, which are of interest for unravelling the structure–activity relationship and the synergistic effect of catalysts down to the atomic level. Exploration of these issues can acquire the connection between catalytic performance and atomic utilization. Typically, the coordination environment of the single metal atom determines the catalytic performance of SACs, while also achieving 100% atomic utilization [17, 18]. It is commonly believed that DACs and TACs are respectively the smallest units of bridge and hollow active sites,

Received: December 9, 2024; **Revised:** February 2, 2025
Accepted: February 7, 2025

✉Address correspondence to 995372896@qq.com

which are known as preferred sites of chemical reactions. In reality, the preferred or active sites of DACs and TACs are different for different types of reactions, and changing as the reaction proceeds, indicative of a flexible mechanism [19–21]. The significant effect of the support on double-atom (DA) and triple-atom (TA) in such catalysts governs the two behavioral properties. More strikingly, the production rate of Pt_2 dimers on graphene is respectively 17- and 45-fold higher than those of Pt single atoms and nanoparticles in hydrolytic dehydrogenation of ammonia borane. It is generally assumed that the Pt_2 dimers are in the oxidized form, promoting hydrogen generation [22]. This emphasizes the advantages of precise active sites in the state and number. Combining theoretical calculations with characterization techniques, Wang et al. suggested that the unique reactivity of Fe_2/C_3N_4 for alkene epoxidation is attributed to active oxygen species dissociated from O_2 molecules at the Fe_2 dimer [23]. In the catalyst, two Fe atoms always act as active sites in the overall multi-step reaction. Soon after, a series of density functional theory (DFT) calculations on TM_2/C_2N (TM = transition metal) for nitrogen reduction reaction (NRR) revealed that the bridge site of TM_2 preferentially adsorbs N_2 and promotes the protonation reaction [19]. In the reduction of N_2 to NH_3, the protonation alternately occurs between the two N atoms at the top sites. This evidences the change of active sites during electrochemical cycling. Furthermore, oxidized Ag_3 trimers on Al_2O_3 were found to be more active and selective for epoxidation than the Ag surface at low temperatures [24]. During the reaction, the oxygen species is pushed to the top site, facilitating the capture of propylene. Later experiments showed that Ru_3 on CN sheets exhibits more excellent catalytic activity and higher chemoselectivity than SACs in the oxidation of 2-aminobenzylalcohol. The high flexibility of Ru_3 results in that one Ru atom connects with both hydroxyl and amino groups, indicating single point adsorption rather than central adsorption [25]. Besides, DFT calculations are expected to be able to guide the design of efficient TACs. For example, Liu et al. designed an Au_3/TiO_2 catalyst for the CO oxidation, following a Langmuir–Hinshelwood mechanism. Specifically, on the top sites of Au_3, one CO reactant acts as a promoter to trigger the formation of two CO_2 molecules as products [26]. After that, a Fe_3/Al_2O_3 catalyst for NRR was proposed. The catalyst utilizes the multi-step redox capability of Fe_3 to promote the decomposition of N_2 and enhance the N_2 conversion to NH_3 [20]. Most of these studies on DACs and TACs focused on the activity and selectivity of the reaction, with little specific discussion on the atomic utilization.

Going back to the basics, the atomic utilization efficiency is defined as the ratio of the metal atoms involved in a chemical reaction to all the constituent metal atoms in a catalyst. Note that the chemical/electrochemical reaction could be either a one-step reaction or a multi-step reaction. In the former case, the atomic utilization of catalysts is clear because the active site comprises all metal atoms involved. In the latter case, the situation is more complex because the active sites will constantly change as the reaction progresses. In this connection, it is prescriptive that the numerator of the ratio is the sum of metal atoms involved in each step of the reaction. Of course, the metal atoms of catalysts should ensure the completion of the intended chemical reaction. The definition can provide a unified standard for comparison among ADMCs, making the problem straightforward. According to this definition, we deduce that DACs similar to SACs can achieve 100% atom utilization [19, 22, 23], while TACs may only have a lower atom utilization of about 1/3 [24, 25] or 2/3 [26] in multi-step reactions. All in all, the electronic properties of active sites composed of multiple metal atoms of a catalyst determine the activity or selectivity of the reaction, while the (morphological) change of active sites during the reaction governs the atomic utilization. In principle, as the number of metal atoms of ADMCs increases, the change of active sites during the reaction tends to be gentle, and the atomic utilization efficiency decreases. Under the premise of ensuring catalytic activity, from the ratio of active sites to constituent atoms in a catalyst, by definition we believe that fully exposed cluster catalysts containing only a few atoms [27–29] cannot have a higher atomic utilization than TACs—let alone SACs. The reason is that from a functional perspective, part of the constituent atoms can be completely independent of active sites in a cluster catalyst. In addition to the activity and selectivity, the atomic utilization has always been a matter of concern from an economic point of view. As far as current research is concerned, both catalytic performance and atomic utilization, derived from the state, number and distribution of active sites relative to the constituent atoms, indicate that DACs and TACs are closer to SACs than atomically dispersed cluster catalysts. All of these findings suggest that a further subdivision of ADMCs into FACs (rather than just SACs) and cluster catalysts is necessary and beneficial for a better understanding of the mechanism and essence of catalytic reactions at the atomic level. With the aim of revealing the flexible dependence of active sites on the constituent atoms in the elementary reaction, the hydrogen evolution reaction (HER) with a single electron transfer is considered here. The information obtained is helpful for understanding the structure–activity relationship and the synergistic effect at the microscopic level. Meanwhile, this work can also open up the prospects for developing inexpensive hydrogen evolution catalysts for clean energy conversion. Earlier experiments showed that TiO_2-supported Ni nanoparticles [30] and clusters [31] can been considered as stable and low-cost photocatalysts for hydrogen production. In the former, the 0.5 wt.% Ni/TiO_2 photocatalyst displays superior photocatalytic activity to a 2 wt.% Au/TiO_2 reference one at low ethanol concentrations (1 vol.%–15 vol.%), while in the latter, Ni_n ($10 < n < 20$) clusters on the TiO_2 surface facilitate a thermal evolution of H_2 at room temperature, similarly as observed for Pt clusters. Our recent series of studies on SACs, DACs and TACs indicated that the hydrogen evolution activity and atomic utilization vary irregularly with the number of central metal atoms, and meanwhile, the active sites are constantly changing as well [32–34]. In principle, it is believed that TiO_2-upported single-atom (SA) and clusters or nanoparticles are at opposite ends of a size spectrum. However, considering the facts that the size of aggregates in FACs is at the atomic level and the catalytic activity is mainly determined by the coordination environment of central metal atoms, we believe that analyzing the size dependence of the catalytic activity and atomic utilization efficiency of FACs is no longer suitable and convenient.

Breaking with standard conventions, for ADMCs we shift our focus to the dependence of the catalytic performance on the number of metal atoms instead of the size of a metal ensemble. As a rational extension to a previously reported series of FACs with varying the number of Ni atoms from 1 to 3 (i.e., SACs/DACs/TACs), a system with a Ni_4 tetramer on TiO_2 (Ni_4/TiO_2) is created as a representative of quadruple-atom catalysts (QACs). Using DFT calculations, we first investigate the growth

habit of Ni_4 tetramer on TiO_2 following a bottom-up approach and then assess the structural stability of all possible Ni_4/TiO_2. The purpose is to demonstrate whether TM tetramers can be synthesized on the anatase TiO_2 (101) surface by the metal ion implantation and deposition method [35, 36]. Secondly, we analyze the structural and binding characteristics, and valence state distribution of metals of two structurally different Ni_4/TiO_2 for a comparative study on evaluating the dependence of active sites on the constituent atoms (for the atomic utilization) in HER. The active sites, catalytic activity, reaction pathways and mechanisms of hydrogen production of the two Ni_4/TiO_2 are explored. Finally, based on the atomic utilization and catalytic activity, a precise definition is given for FACs by featuring the coordination environment of central metal atoms, which is associated with quantum confinement effect.

2 Computational methods

All spin-polarized DFT calculations on Ni_4/TiO_2 complexes, involving the structural stability and diversity, electronic and valence states, and catalytic activity, were performed using the Vienna *ab initio* simulation package (VASP) [37, 38], with the revised Perdew–Burke–Ernzerhof (rPBE) generalized gradient approximation (GGA) for the electron exchange-correlation potential [39]. The projector augmented wave (PAW) method was adopted for the core electrons [40], and the energy cutoff of 500 eV was employed for the plane-wave basis set to represent the wave functions of the valence electrons. The DFT + U approach was taken to address the on-site Coulomb interactions in the localized d or f orbitals of transition metal compounds [41, 42]. Concretely speaking, an additional Hubbard-type U term with an effective value of 7 eV was considered for the Ti atom, yielding reasonable lattice constants and band gap that are close to the experimental data of anatase TiO_2 [43]. The dipole correction was applied to decouple the electrostatic interaction between the periodic slabs, with a vacuum thickness of ~ 15 Å along the z direction. The Brillouin zone was sampled by a 3 × 3 × 1 mesh of k-points in the Monkhorst–Pack scheme [44], which was also used for the vibrational frequency calculations.

A slab of three Ti_2O_4 layers, extracted from the optimized anatase crystalline phase, was chosen to mimic the TiO_2 (101) surface (see the left panel of Fig. 1). Regarding supported Ni aggregates, all coordinatively unsaturated O_{2c} (2-fold coordinated O) and Ti_{5c} (5-fold coordinated Ti), and coordinatively saturated Ti_{6c} (6-fold coordinated Ti) and O_{3c} (3-fold coordinated O) sites/atoms (labeled with numbers of 4 to 16 in Fig. 1) were highlighted to depict the surface groove or step and cavity. To maintain comparability with other studies on FACs, ranging from SACs and DACs to TACs [32–34], a p (2 × 2) supercell containing a Ni_n (n = 1–3) unit at the centre of the surface was adopted for this study. It is important to note that as shown in the right panel of Fig. 1, on the surface the distance between the Ni atoms in adjacent unit cells of these FACs remains at least 5.27 Å mainly along the [010] direction, and more especially, the value is much smaller than those along other directions (> 8.86 Å). Therefore, it is generally believed that the size of a (2 × 2) supercell, relative to the dimensions of geometric objects (TM_n) on TiO_2, is sufficient to ensure that all TM_n (e.g., tetramers) originated from the preformed TM_{n-1} (e.g., trimer) can be treated as independent individuals in the simulations. The central Ni atoms in the trimer were labeled with numbers of 1 to 3 in Fig. 1. The top two layers of Ti_2O_4 and the adsorbents of Ni and H were allowed to relax, whereas the bottom one layer of Ti_2O_4 was frozen in all calculations. The energy and force convergence criteria were set to 10^{-6} eV and 0.02 eV/Å, respectively.

Following the assembly of metal aggregates by atom-by-atom deposition or precipitation on the support [31, 45, 46], the relative stability of the isomers of Ni_n on TiO_2 could be estimated by computing the binding energy of the Ni atom on Ni_{n-1}/TiO_2 as below

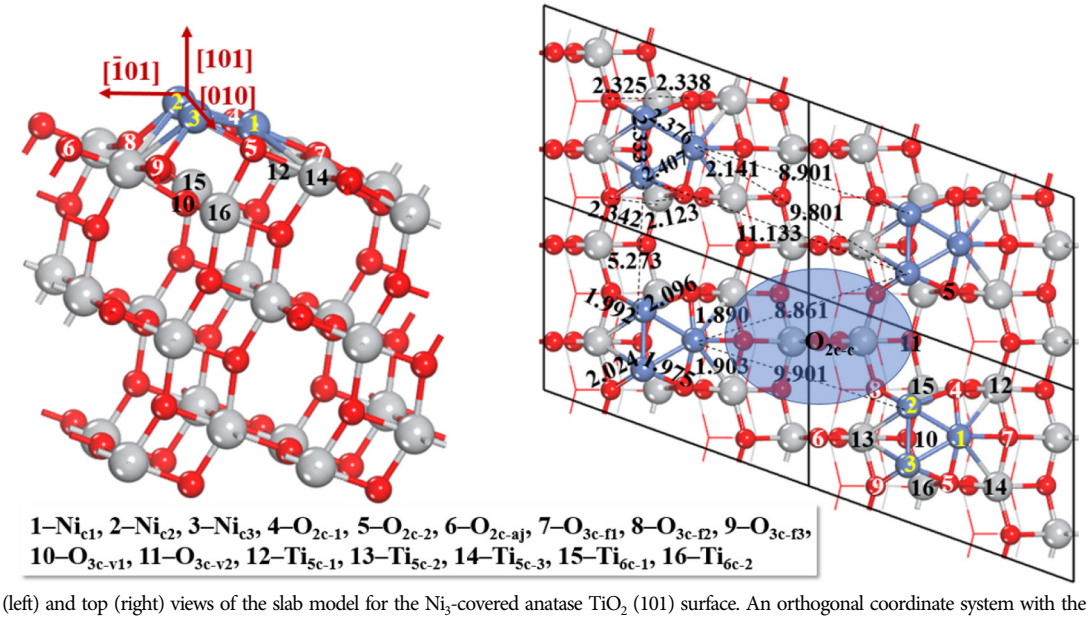

Figure 1 Side (left) and top (right) views of the slab model for the Ni_3-covered anatase TiO_2 (101) surface. An orthogonal coordinate system with the [010], [$\bar{1}$01] and [101] directions in anatase TiO_2 structure is presented in the side view. In the top view, where only the topmost Ti_2O_4 layer containing a Ni_3 trimer at the centre is shown for visualization, the p (2 × 2) supercell indicated by the black rhombus is doubled to compute the distances between the Ni atoms in adjacent unit cells. Some relevant interatomic distances and selected bond lengths (in Å) are highlighted. On the anatase (101) surface, the Ni atoms in the trimer are labeled with numbers of from 1 to 3, and coordinatively unsaturated and saturated Ti and O atoms surrounding or near the central Ni_3 trimer are labeled with numbers of from 4 to 16. The atom numbering is shown in the inset. Blue, gray and red balls represent Ni, Ti and O atoms, respectively.

$$E_{\text{binding}} = E_{\text{Ni}_n/\text{TiO}_2} - (E_{\text{Ni}_{n-1}/\text{TiO}_2} + E_{\text{Ni}}) \quad (1)$$

where $E_{\text{Ni}_n/\text{TiO}_2}$ and $E_{\text{Ni}_{n-1}/\text{TiO}_2}$ are the total energies of Ni_n/TiO_2 and $\text{Ni}_{n-1}/\text{TiO}_2$, respectively. E_{Ni} is the DFT energy of single Ni atom. In principle, the relative stability is compatible with the growth habit of metal aggregates on a surface.

According to the kinetic model of HER provided by Nørskov et al. [47], the adsorption energy of H in each step of the Volmer–Heyrovsky or Volmer–Tafel reactions could be used as a universal descriptor to evaluate the hydrogen production activity of the catalyst. Specifically, the differential H adsorption energy ΔE_{H} as a function of the hydrogen coverage (θ_{H^*}) on Ni_4/TiO_2 was calculated using the following formula [48]

$$\Delta E_{\text{H}} = E_{\text{Ni}_4/\text{TiO}_2} - E_{\text{Ni}_4/\text{TiO}_2+(n-1)\text{H}} - E(\text{H}_2)/2 \quad (2)$$

where $E_{\text{Ni}_4/\text{TiO}_2+n\text{H}}$ and $E_{\text{Ni}_4/\text{TiO}_2+(n-1)\text{H}}$ are the total energies of Ni_4/TiO_2 with n and (n–1) H atoms, respectively. $E(\text{H}_2)$ is the DFT energy of a free H_2 molecule. The Gibbs free energy of H adsorption, ΔG_{H^*}, at each reaction step, following the computational hydrogen electrode model under the constant charge approximation without considering explicit solvent [49], was achieved as follows

$$\Delta G_{\text{H}^*} = \Delta E_{\text{H}} + \Delta E_{\text{ZPE}} - T\Delta S_{\text{H}} + \Delta G_U \quad (3)$$

where ΔE_{ZPE} and ΔS_{H} are the differences in zero point energy (ZPE) and H entropy between the H-adsorbed state and the gas phase at standard conditions. Our DFT calculations indicated that ΔE_{ZPE} are 0.04 and 0.09 eV for the adsorbed H on all Ni_4 isomers and the coordinatively unsaturated O_{2c} of TiO_2, respectively, which are compatible with the chemical nature of H–TM [47] and H–S bonds [48]. $T\Delta S_{\text{H}}$ was obtained to be ca. –0.20 eV at 300 K and 1 bar, with the entropy of gaseous H_2 in standard states. T is the HER temperature. ΔG_U is the free energy change with respect to the applied potential U and the number of varied electrons n (ΔG_U = $-neU$). Note that more information about the thermodynamic stability of Ni_4/TiO_2, Bader charges of all central Ni atoms and adsorbed H species in the HER process and total and local density of states (DOS) of Ni_4/TiO_2 at full H coverage can be seen in the Electronic Supplementary Material (ESM).

3 Results and discussion

The bottom-up synthetic strategy and orientation relationship of few-atom systems on TiO_2 [14, 16, 32–34] demonstrate that the Ni_3 trimer can be taken as a reference embryo or seed of supported nanoparticles. Considering the overall structural characteristics of Ni_3-covered TiO_2, we now introduce an orthogonal coordinate system to study the growth habit of Ni_4 tetramer on the anatase (101) surface. As depicted in the left panel of Fig. 1, the [010] and [$\bar{1}$01] directions are respectively parallel to and perpendicular to the oxygen-binding groove and/or the Ni_{c2}–Ni_{c3} dimer step, both of which are in the basal plane—(101) surface, and the [101] direction is normal to the anatase TiO_2 (101) surface (i.e., the z direction). The coordinate origin is located at the center of the reference Ni_3 seed. After detecting all possible adsorption or deposition sites for metal-vapor atoms or reduced metal atoms around the Ni_3 seed, we find three metastable and stable isomers of Ni_4 tetramer on TiO_2. It should be remembered that the [010], [$\bar{1}$01] and [101] axes respectively correspond to three different growth directions of Ni_4 on TiO_2, and meanwhile, for all optimized structures only positive frequencies are observed in the vibrational frequency calculations, indicating high dynamic stability. The three isomers of Ni_4 are linear-chain, rhombic and tetrahedral structures, respectively, as depicted in Fig. 2. Correspondingly, the calculated binding energies are −2.36, −3.28 and −3.53 eV, all of which not only reveal that the three isomers are energetically stable, but also disclose that the order of the relative stability of Ni_4 on TiO_2 is linear-chain < rhombus < tetrahedron. The negative binding energy signifies that once a single Ni atom (within the prescribed distance range), no matter which direction it comes from, approaches the trimer, it will be captured by the Ni_3 seed, eventually form a Ni_4 tetramer on the surface (no

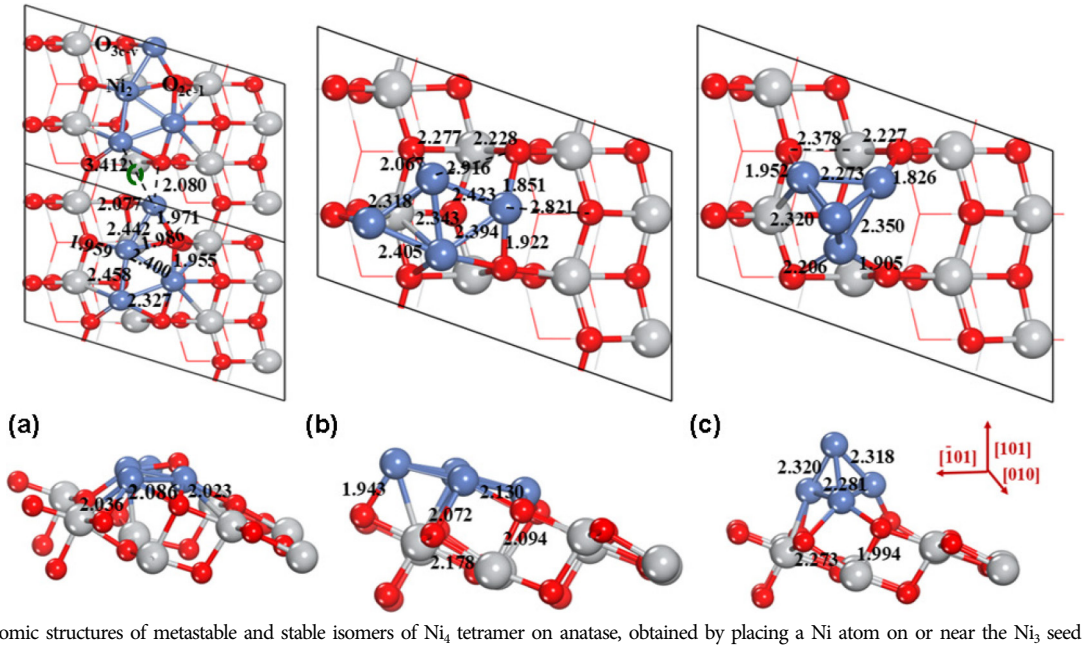

Figure 2 (a) Atomic structures of metastable and stable isomers of Ni_4 tetramer on anatase, obtained by placing a Ni atom on or near the Ni_3 seed along different coordinate axes. (a) Linear-chain along the [010] direction, (b) rhombus along the [$\bar{1}$01] direction, and (c) tetrahedron along the [101] direction. Selected bond lengths (in Å) are highlighted. In (a), a p (2 × 4) unit cell is provided for visualization, while others in (b) and (c) remain unchanged to be a p (2 × 2) unit cell.

geometric restrictions impede this process). This result indicates that the self-assembly of Ni atoms on oxides is a spontaneous process, and the driving force is the local attraction of the seed/surface to reduced Ni atoms, both of which are consistent with previous reports on Ni clusters or nanoparticles on TiO_2 [30, 50, 51]. This suggests the feasibility and potential of a universal bottom-up method for preparing FACs, as being used in the synthesis of ADMCs [16, 52, 53]. Different atomic arrangements of Ni_4 tetramers on TiO_2 regarding the [010], [$\bar{1}$01] and [101] axes are known as the growth anisotropy of few-atom systems on oxides. Intuitively, the isomers of Ni_4 on TiO_2 can be divided into two categories: planar and tetrahedral structures, according to whether the condensation of Ni_{c4} onto the Ni_3 trimer depends on the anatase (101) surface or not.

More precisely, there are two planar atom arrangement structures of Ni_4 tetramer on TiO_2, which are respectively dependent on the surface O-cavity for linear-chain (Fig. 2(a)) and the metal dimer step for rhombus (Fig. 2(b)) by chemical bonding. In comparison, the surface stress induced by the trimer seed only plays an auxiliary role in the anisotropic growth of Ni_4 on TiO_2. Typically, the surface O-cavities adjacent to the Ni_3 trimer are generally enlarged. The Ni_{c4} atom would successfully fall into the adjacent surface O-cavity, but could only bind to one Ni atom of the trimer, and coordinate to two partially saturated O_{2c}. It is a bit like the situation of the Ni_{c1}. But their bond lengths are 1.971 and 2.080 Å (Fig. 2(a)), respectively, slightly smaller than those of Ni_{c1}–$O_{2c\text{-}1}$ (1.955 Å) and Ni_{c1}–$O_{2c\text{-}2}$ (2.023 Å) (note that the Ni_{c1} could be taken as the sample of SACs [32]). The length of Ni_{c4}–Ni_{c2} is 2.442 Å, which is between the Ni–Ni lengths of the Ni_3 trimer (2.327–2.458 Å), but much smaller than the distance of Ni_{c4} from the Ni_{c3} of the trimer along the [010] direction (3.412 Å). It is a dispersed linear-chain tetramer, also exhibiting a non-close-packed arrangement. Looking further we see that such a large interatomic distance would allow for the fabrication of one-dimensional (1D) linear-chain nanostructures, by inserting a single Ni atom (in the groove) between Ni_{c4} and Ni_{c3} (represented by a green dashed circle in Fig. 2(a)). In that case, the growth of 1D metal nanostructures is completely dependent on oxygen-binding grooves and surface cavities that are staggered and arranged in parallel. It can be anticipated that the 1D nanostructures with narrow width and weak coordination affinity would show a unique pattern and have in-plane quantum effects (e.g., confinement and tunneling), making them attractive for the use in electronic communication, detection and characterization [54, 55].

Nevertheless, the Ni_4 tetramer preferentially grows along the [$\bar{1}$01] direction for a rhombic atom arrangement structure on TiO_2. The deposited Ni_{c4} atom is coordinated to the Ni_{c2} and Ni_{c3} atoms of the dimer step, forming two Ni–Ni bonds, and the coordinatively unsaturated $O_{2c\text{-}aj}$ of the adjacent surface cavity. As depicted in Fig. 2(b), the lengths of Ni_{c4}–Ni_{c2} (2.318 Å) and Ni_{c4}–Ni_{c3} (2.405 Å) are smaller than or close to those of the Ni_3 seed (2.333–2.407 Å), and the Ni_{c4}–O_{2c} length (1.943 Å) is slightly larger than those of Ni_{c1}–O_{2c} (1.851 and 1.922 Å). The former confirms the dominant role of the metal–metal bond compared with the metal–O bond in stabilizing the planar Ni_4 tetramer on anatase TiO_2, consistent with the order of the binding energy. The latter is compatible with the result of SA/TiO_2 catalysts, which the metal atom is at the center of the surface cavity [56–58]. Moreover, thanks to the open availability of the dimer step, the deformation energy can be negligible compared to the Ni_{c4}–O_{2c} bond energy in the formation of Ni_4, successfully resulting in the movement of the Ni_3 seed to the left oxygen-binding groove. It must be said that this is an unexpected result, suggesting a unique support interaction that is influenced by the coordination environment of central metal atoms. By contrast, the tetrahedral Ni_4 tetramer on TiO_2 can be readily achieved by the adsorption or deposition of Ni at the hollow site of the trimer along the [101] direction. In this structure, there are only three new Ni–Ni bonds by coordinating with the Ni_3 trimer. From Fig. 2(c), we see that the lengths of these bonds are respectively 2.318 Å (for Ni_{c4}–Ni_{c1}), 2.320 Å (for Ni_{c4}–Ni_{c2}) and 2.281 Å (for Ni_{c4}–Ni_{c3}), and the length of each side of the triangular base of the tetrahedron does not exceed 2.350 Å. Note that all the Ni–Ni lengths of tetrahedral Ni_4 tetramer as well as two planar structures are smaller than the Ni–Ni distance in bulk Ni (2.492 Å) [59]. This result illustrates a strong self-aggregation ability of universal few-atom systems from the metal–metal bonds. Another strong evidence from thermodynamics is that the binding energies of all Ni_4 tetramers on TiO_2 are weaker than the cohesive energy of Ni clusters (~ −4.67 eV). In reality, the distances between most atoms exceed the prescribed or allowable range in the sample preparation, such as the Ni atoms reduced from the Ni^{2+} ions at the central region of the (4 × 4) supercell, and far from the [010] and [$\bar{1}$01] axes (see the elliptical shaded area in the right panel of Fig. 1). In this case, the kinetic barrier for the long-distance migration of the Ni atom certainly would prevent the condensation of Ni atoms on TiO_2. As the coverage of Ni atoms increases or the distance between two metal atoms decreases, the kinetic inhibition effects become progressively less severe [32], which more readily facilitates the formation of aggregates by the deposition and diffusion mechanism. The most extreme scenario is that even when the Ni_{c4} atom is deposited at the center (i.e., $O_{2c\text{-}c}$) of the elliptical shaded area, it will also eventually diffuse into the center of the adjacent surface O-cavity, just like the case of SA/TiO_2 [56–58], both of which are attributed to the coordination effect of surface O_{2c} with deposited Ni atom. In the TiO_2-supported Ni-SAC, for low coverage (1/4 monolayer), we found an energy barrier of 1.0 eV for the dimerization of Ni atoms on the anatase TiO_2 (101) surface [32]. Compared to that, owing to the greater driving force, it can be expected that the atomic diffusion barrier should be lower for the growth of Ni_4/TiO_2 in the extreme scenario. Therefore, it is a high surface coverage of metal atoms (such as 1 monolayer) that is a necessary condition for FACs but not for SACs. At this point, the ambient temperature required to overcome the diffusion barrier from the breaking of two Ni-O_{2c} bonds for metal aggregation will be lower.

All in all, the anisotropy of surface structure and properties of the support and the intrinsic aggregation effect of metal atoms govern the growth habit of aggregates on oxides. Specific to this study, the tetrahedral structure of Ni_4 is formed first in an island growth mode [60], followed by the rhombic structure and at last linear-chain structure in a layer growth mode [61]. The growth habit points to a competition scenario: the Ni–O bond from support interactions versus the metal–metal bond in Ni_n aggregates. Note that this issue is particularly relevant in the study of size-dependent supported catalysts, but has not been elaborated up to now [1]. We now present a positive result, that is, for Ni_4/TiO_2 the metal–metal bond is superior to the Ni–O bond, which is exactly the opposite of the situation of DACs and TACs [33, 34, 62], but is compatible with the result of metal nanoparticles supported catalysts [63, 64]. An interesting and surprising phenomenon is that the competition

scenario for ADMCs gradually shifts from the Ni–O bond dominance to the Ni–Ni bond dominance with the increase of the number of Ni atoms. There exists a turning point which extracts desired FACs from cluster catalysts in ADMCs. To be precise, it is Ni_4 on TiO_2, which can be either a planar two-dimensional (2D) structure or a volumetric three-dimensional (3D) structure. The delicate energy balance (< 250 meV) may be influenced by kinetic effects in the realistic growth. This means that both rhombic and tetrahedral Ni_4 tetramers can grow well on anatase TiO_2 under certain conditions. Considering the relative stability, steric hindrance and requirement of a close-packed arrangement of metal atoms, we identify the rhombic and tetrahedral Ni_4 tetramers as the main focus in the following discussion about the differentiation of catalyst types. Furthermore, we also perform *ab initio* molecular dynamics (AIMD) simulations in the NVT ensemble within the VASP code to examine the thermodynamic stability of the rhombic and tetrahedral Ni_4 tetramers on TiO_2 in air atmosphere. A (2 × 2) supercell containing a Ni_4 tetramer at the center of the surface was employed as before (see Fig. 1). The time step is taken to be 2 fs and the total time of molecular dynamics (MD) run is 100 ps. After MD run (from 50 to 100 ps), we obtain the results at a range of temperatures from 100 to 300 K and plot some results in Fig. S1 in the ESM. We see that the planar rhombic structure of Ni_4 is stable at a certain temperature (~ 200 K), while the tetrahedral structure is stable at the room temperature on the TiO_2 surface. These results are compatible with the relative stability of Ni_4 on TiO_2 from energetics. Note that considering the protective effect of the ionic liquid, we believe that the planar rhombic Ni_4/TiO_2 might remain thermodynamically stable in the HER process under standard conditions.

Besides that, the property-related structural characteristics (e.g., size, morphology, atomic arrangement etc.) could be used as a complementary tool for identifying and classifying the types of ADMCs. As for supported catalysts, the interfacial bonding characteristics are critically important in determining the overall system performance due to strong metal–support interactions [65]. Here we find that information regarding the property-related structural characteristics for the two Ni_4/TiO_2 is significantly different. More precisely, the four Ni atoms lying flat on the TiO_2 surface preferentially interact with the O atoms in the planar rhombic structure (Fig. 2(b)). There should be six Ni–O bonds according to the reference value (2.084 Å) in bulk NiO, and meanwhile, five surface O atoms complete the coordination environment of all central Ni atoms. Specifically, the Ni_{c1} coordinates with the $O_{2c\text{-}1}$ and $O_{2c\text{-}2}$, the Ni_{c2} coordinates with the $O_{3c\text{-}f2}$, the Ni_{c3} coordinates with the $O_{2c\text{-}2}$ and $O_{3c\text{-}f3}$, and the Ni_{c4} coordinates with the $O_{2c\text{-}aj}$. All coordination bond lengths are between 1.851 Å to 2.072 Å. Thereinto, the Ni_{c4}–$O_{2c\text{-}aj}$ bond would not only stabilize and support the planar structure of Ni_4 by overcoming the surface tension, but also saturate the TiO_2 surface by the electron transfer from Ni_{c4} to $O_{2c\text{-}aj}$. Meanwhile, the Ti_{6c}–O bonds beneath the Ni_4 tetramer are shortened in comparison to those of the Ni_3 seed (Fig. 1(b)), indicative of an increased metallicity of Ni_4, and the Ni_{c1}–$O_{3c\text{-}f1}$ and Ni_{c2}–$O_{2c\text{-}1}$ bonds on the surface are respectively elongated to 2.821 Å from 2.141 Å and 2.916 Å from 2.096 Å, suggesting that $O_{3c\text{-}f1}$ and $O_{2c\text{-}1}$ do not participate in coordination. The Ni_4 tetramer appears closer to the groove and farther from the cavity. While in the tetrahedral structure of supported Ni_4 (Fig. 2(c)), we see that only the Ni atoms of the trimer seed interact with the TiO_2 support, creating four Ni–O bonds. A striking phenomenon is that the basal plane of the tetrahedron has rotated and the coordination environment exclusively from surface O atoms has changed during the transition from trimer to tetramer by receiving a deposited Ni atom. The Ni_{c1} coordinates to the $O_{2c\text{-}1}$ with a bond length of 1.826 Å, the Ni_{c2} coordinates to the $O_{3c\text{-}f2}$ with a bond length of 1.952 Å, and the Ni_{c3} coordinates to the $O_{2c\text{-}2}$ and $O_{3c\text{-}3}$ with two Ni–O bond lengths of 1.905 and 2.206 Å; whereas, in the trimer seed (Fig. 1) the Ni_{c1} coordinates to the $O_{2c\text{-}1}$ and $O_{2c\text{-}2}$ (with two Ni–O bond lengths of 1.890 and 1.903 Å, the Ni_{c2} coordinates to the $O_{3c\text{-}f2}$ and $O_{2c\text{-}1}$ (with two Ni–O bond lengths of 1.992 and 2.096 Å), and the Ni_{c3} coordinates to the $O_{2c\text{-}2}$ and $O_{3c\text{-}3}$ (with two Ni–O bond lengths of 1.975 and 2.024 Å). Roughly speaking, the interfacial bonding characteristics of the tetrahedral Ni_4 tetramer are somewhat similar to those of the Ni_3 trimer on TiO_2 [34].

The Bader charges of all central Ni atoms and coordination O atoms in the two Ni_4/TiO_2, relative to the reference Ni_3/TiO_2, are listed in Table 1. First of all, we see that the electron transfer from Ni_4/Ni_3 to TiO_2 through Ni–O bonds causes partial saturation of surface O_{2c} atoms by accepting electrons, and meanwhile makes the supported aggregate be cationic by donating electrons, which is the same as the result of oxide-supported metal nanoparticle catalysts [66]. We go a step further by looking at the Ni_3 trimer and the planar Ni_4 tetramer on TiO_2, and find that the Ni_{c1} always donates the most electrons (~ 0.5 e) to the support, exhibiting the highest oxidation state compared with other Ni atoms (~ 0.2–0.3 e); whereas in the tetrahedral Ni_4 tetramer, the Ni_{c3} with two coordination O atoms instead of the Ni_{c1} with one coordination O atom gives more electrons, due to the rotation of the basal plane. More strikingly, these results from Bader charge analysis imply that for the immobilized FACs in a planar atom arrangement, the single-atom configuration is the most stable, relative to the rhombic tetramer, triangle trimer and linear dimer. All four central Ni are cations. By contrast, in the tetrahedral Ni_4 tetramer, only the triangular basal plane remains cationic ($+\delta$ valence state, corresponding to the loss of ~ 0.3–0.5 e), while the Ni_{c4} at the hollow of the Ni_3 seed is in a zero-valence state (0), regardless of support interactions. Relatively speaking, the Bader charges of coordination O atoms of the TiO_2 surface remain unchanged. The sharp contrast in the electron distribution reveals the essence of FACs or ADMCs. That is, the metal aggregate, not the TiO_2 support, dominates and initiates the catalytic reaction, and unsurprisingly, different metal valence state distribution of aggregates would lead to different active sites and reaction mechanisms. At first glance, we believe that the planar rhombic Ni_4/TiO_2 could be categorized as a FAC similar to SACs and DACs [14, 15], in all of which the aggregate can be functioned as an

Table 1 Bader charges of all central Ni atoms and coordination O atoms in the two Ni_4/TiO_2, relative to the Ni_3/TiO_2 system (in unit of e)

	$O_{2c\text{-}1}$	$O_{2c\text{-}2}$	$O_{2c\text{-}3}$	$O_{3c\text{-}f1}$	$O_{3c\text{-}f2}$	$O_{3c\text{-}v}$	Ni_{c1}	Ni_{c2}	Ni_{c3}	Ni_{c4}
Ni_3/TiO_2	7.25	7.19	7.12	7.32	7.29	7.28	9.51	9.65	9.63	
Ni_4/TiO_2 (planar)	7.25	7.23	7.18	7.33	7.30	7.30	9.44	9.80	9.71	9.75
Ni_4/TiO_2 (tetrahedral)	7.25	7.21	7.13	7.32	7.29	7.29	9.58	9.73	9.48	10.04

enlarged metal-like pseudo-atom; while the tetrahedral Ni_4/TiO_2 is a standard atomically precise metal cluster catalyst [4, 8].

For the sake of simplicity and intuitiveness, the HER is used as a probe to confirm the performance differences between the two Ni_4/TiO_2. Meanwhile, the purpose of the probe experiment is to estimate the atomic utilization of the two types of catalysts, by figuring out the relationship between the active sites/reaction pathways and catalytic efficiency. After thoroughly searching the adsorption sites of H species on Ni_4/TiO_2, which include the top, bridge and hollow sites of Ni_4 tetramer and Ni–O bonds, we identify the stable H adsorption structures at different H coverages, as depicted in Figs. 3 and 4. It can be seen that there are respectively three and four H species adsorbed on the planar rhombic structure and the tetrahedral structure. In the latter, the extra H is derived from the hydroxylation reaction at the interface, indicating that the H on $O_{2c\text{-}2}$ possesses 0.3–0.4 e throughout the entire reaction process (see Fig. 4(a) and Table S1 in the ESM). This result is the same as the results of SACs and DACs [32, 33]. All of these are associated with the weak coordination effect between TiO_2 and aggregates. The other three H are adsorbed on the Ni_4 tetramer, being the atomic valence state (see Table S1 in the ESM). By contrast, thanks to the moderate oxidation states ($+\delta$) of all Ni atoms in the planar rhombic structure, the H atoms are adsorbed on the Ni_4 tetramer, regardless of the TiO_2 support. This result is the same as the result of TACs [34], which is attributed to the strong coordination effect between TiO_2 and Ni_4 rhombus. According to the Eq. (2), we introduce now a variable surface coverage of H on Ni_4/TiO_2, θ_{H^*}, by adding H atoms one by one. Essentially and practically, the $H–O_{2c\text{-}2}$ does not participate in hydrogen production [46, 58], so it is excluded in the following discussion. For the sake of clarity and consistency, the first, second and third adsorbed H atoms on the Ni_4 tetramer are respectively denoted by H^*_{ad1}, H^*_{ad2} and H^*_{ad3} in two structurally different Ni_4/TiO_2. Accordingly, 1H, 2H and 3H adsorption scenarios also correspond to θ_{H^*} = 1/3, 2/3, and 1 monolayers, respectively.

In the planar rhombic structure of Ni_4/TiO_2, the H^*_{ad1} atom prefers to be at the hollow site (Hol_1) of the left triangle, but slightly off-center with the $H–Ni_{c2}$, $H–Ni_{c3}$ and $H–Ni_{c4}$ lengths of 1.867, 1.726 and 1.650 Å. This result is somewhat different from the result of H-adsorbed Ni_3/TiO_2, which the H^*_{ad1} is located at the bridge site of $Ni_{c2}–Ni_{c3}$ edge in the groove [34]. Meanwhile, except for the $Ni_{c4}–O_{2c\text{-}aj}$ and $Ni_{c3}–Ni_{c4}$ bonds, the other bond lengths change very little, as compared with the planar rhombic Ni_4/TiO_2. As the H^*_{ad2} atom is adsorbed at the hollow site (Hol_2) of the right triangle as always, the H^*_{ad1} is pushed away from the Hol_1 to the bridge site of the $Ni_{c3}–Ni_{c4}$ edge and further outward to the interfacial O, indicative of a repulsion between H^*_{ad1} and H^*_{ad2}. Interestingly, this is similar to the result of 2H adsorption scenario of Ni_3/TiO_2 [34]. The bond lengths of $H^*_{ad1}–Ni_{c3}$ and $H^*_{ad1}–Ni_{c4}$ are decreased to 1.632 and 1.601 Å, respectively. For H^*_{ad2} at the Hol_2 site, the bond lengths are as follows: 1.789 Å ($H^*_{ad2}–Ni_{c1}$), 1.685 Å ($H^*_{ad2}–Ni_{c2}$) and 1.672 Å ($H^*_{ad2}–Ni_{c3}$). The $Ni_{c4}–O_{2c\text{-}aj}$ length is further shortened, and the $Ni_{c3}–Ni_{c4}$ length is also elongated. Finally, the H^*_{ad3} can only sit at the bridge site of the $Ni_{c2}–Ni_{c4}$ edge, with the lengths of 1.605 Å for $H^*_{ad3}–Ni_{c2}$ and 1.585 Å for $H^*_{ad3}–Ni_{c4}$. The H^*_{ad2} atom is still trapped at the Hol_2 site but with slightly shortened bond lengths, just like the case of H-adsorbed bulk Ni. The lengths of $Ni_{c4}–O_{2c\text{-}aj}$ and $Ni_{c3}–Ni_{c4}$ bonds that involve H^*_{ad1} are elongated. It is obvious that at θ_{H^*} = 1 monolayer the adsorption configuration of H-adsorbed Ni_4/TiO_2 is quite different from that of H-adsorbed Ni_3/TiO_2, which all three edges of the triangle are occupied by the H atoms [34]. This structure-dependent performance (i.e., the reduction-adsorption of H^+) can distinguish the essential differences between trimer and tetramer in the reaction. The calculated adsorption energies of H^*_{ad1}, H^*_{ad2} and H^*_{ad3} are −3.07, −2.54, and −2.54 eV at θ_{H^*} = 1/3, 2/3 and 1 monolayers, respectively. Compared to that, the situation of the tetrahedral Ni_4/TiO_2 is simpler. Figures 4(b)–4(d) show that the three H atoms are sequentially adsorbed at the $Ni_{c1}–Ni_{c4}$, $Ni_{c2}–Ni_{c4}$ and $Ni_{c3}–Ni_{c4}$ edges, emphasizing the pivotal role of the Ni_{c4} atom in HER. This adsorption sequence somewhat reflects the repulsion between $H^*_{ad1,ad2,ad3}$ and $H–O_{2c\text{-}2}$, not only indicating a steric

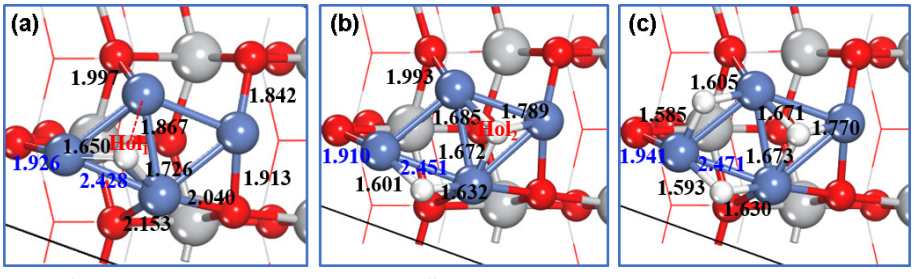

Figure 3 Adsorption structures of H on the planar rhombic Ni_4/TiO_2 at different H coverages. (a) 1H adsorption (1/3 monolayer) scenario, (b) 2H adsorption (2/3 monolayer) scenario, and (c) 3H adsorption (1 monolayer) scenario. Lengths of selected bonds are indicated. Blue, white, gray and red balls represent Ni, H, Ti and O atoms.

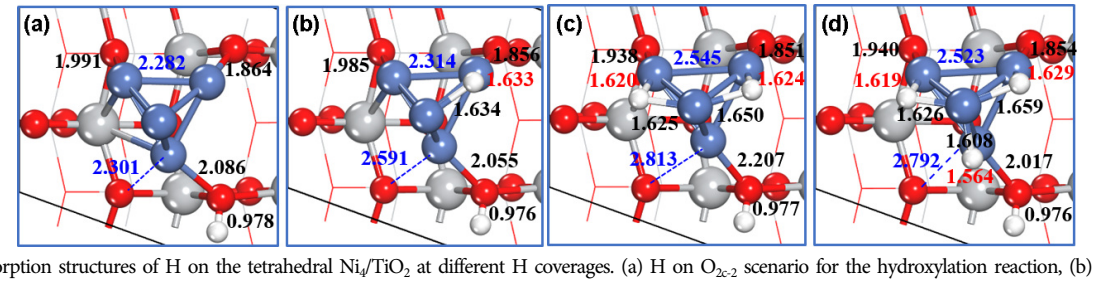

Figure 4 Adsorption structures of H on the tetrahedral Ni_4/TiO_2 at different H coverages. (a) H on $O_{2c\text{-}2}$ scenario for the hydroxylation reaction, (b) 1H adsorption (1/3 monolayer), (c) 2H adsorption (2/3 monolayer), and (d) 3H adsorption (1 monolayer) on the metal tetramer scenarios. Lengths of selected bonds are indicated. Blue, white, gray and red balls represent Ni, H, Ti and O atoms.

hindrance effect but also demonstrating a surface saturation effect. The bond lengths of H–Ni remain between 1.620–1.659 Å, except for H^*_{ad3} with shortened bond lengths (1.608 and 1.564 Å for H^*_{ad3}–$Ni_{c3,c4}$) because it is closer to the H–$O_{2c\text{-}2}$ than other H atoms. Correspondingly, the calculated adsorption energies of H^*_{ad1}, H^*_{ad2}, and H^*_{ad3} on the tetrahedral Ni_4/TiO_2 are −2.51, −2.87, and −2.36 eV at θ_{H^*} = 1/3, 2/3 and 1 monolayers, respectively. Another noteworthy result is the sharp increase in the distance between Ni_{c3} and $O_{3c\text{-}f3}$ in the reduction-adsorption process. It means that HER on the tetrahedral Ni_4/TiO_2 would be independent of the effects of the $O_{3c\text{-}f3}$, both containing mechanical support and chemical coordination.

The structure-dependent performance can be further reflected in the HER activity and mechanism or pathway by calculating the Gibbs free energy of H adsorption, (ΔG_{H^*}), in each step of HER. Figures 5 and 6 depict the Gibbs free energy diagrams of Volmer–Heyrovsky and Volmer–Tafel reactions on the two Ni_4/TiO_2 at different H coverages (θ_{H^*} = 1/3, 2/3 and 1 monolayers). Thermochemistry suggests that very small $|\Delta G_{H^*}|$ corresponds to an excellent HER catalyst, at which all the elementary steps of the Volmer–Heyrovsky or Volmer–Tafel mechanism are easy to proceed under standard conditions [47].

From Fig. 5(a), we see that for the planar rhombic Ni_4/TiO_2, at θ_{H^*} = 1/3 monolayer, too negative free energy (−0.55 eV) means that the reduction reaction of $H^+ + e^- \rightarrow H^*$ is easy to occur at the Ni_{c3}–Ni_{c4} edge, especially forming an H–Ni moiety with strong s–d hybrid bonds (see Fig. S4 in the ESM). A serious consequence of this is that high electronic localization blocks the electron transfer from the H–Ni moiety to the H^+ from solution, thereby inhibiting the Heyrovsky reaction. Even at higher coverage (2/3 monolayer), the $H^*_{ad1} + H^*_{ad2}$ combination still does not proceed catalytically, due to too high ΔG_{H^*} (0.56 eV). Instead, the H–Ni moiety would yield two unexpected benefits: the Ni_{c2} is free and the reduction ability of the H^*_{ad1}-passivated Ni_4 is sharply decreased. The Ni_{c2}–Ni_{c4} edge becomes a more favorable active site for the H^*_{ad3} reduction and then makes H^*_{ad3} act as a site to capture and reduce H^+, finally achieving $H^+ + e^- + H^* \rightarrow H_2$ at θ_{H^*} = 1 monolayer. More strikingly, the $|\Delta G_{H^*}|$ of the overall Volmer–Heyrovsky process is close to zero (marked by the red arrow in Fig. 5(b)), indicating that HER is almost thermo-neutral. Even though following the Volmer–Tafel mechanism, the $H^*_{ad2} + H^*_{ad3}$ combination can be carried out well due to the $|\Delta G_{H^*}|$ smaller than 0.02 eV. The uphill step implies that the hydrogen production is an endothermic process. The same result is also observed in HER using H^*_{ad2} (at the HOl_2) as an active site to completely reduce H^+ from solution, following the Volmer–Heyrovsky mechanism. In brief, we believe that the planar rhombic Ni_4/TiO_2 provides two available sites and two reaction pathways for hydrogen production, with the highest activities (originated from $|\Delta G_{H^*}|$). These values are very close to that of Pt at 1 monolayer coverage of H (−0.03 eV) [67]. Following the Volmer–Heyrovsky pathway, the dual-site reaction mechanism would double the hydrogen production rate, so we consider that the atomic utilization efficiency is 1/2. Further taking into account the addition of the Volmer–Tafel pathway for the hydrogen evolution process occurring with the two H atoms, we believe that the atomic utilization efficiency of the planar rhombic Ni_4/TiO_2 could reach 3/4, which may approach 100% atomic utilization of SACs.

For the tetrahedral Ni_4/TiO_2, the situation is not so good. From Fig. 6(a), we see only when the H^*_{ad1} at the bridge site of the

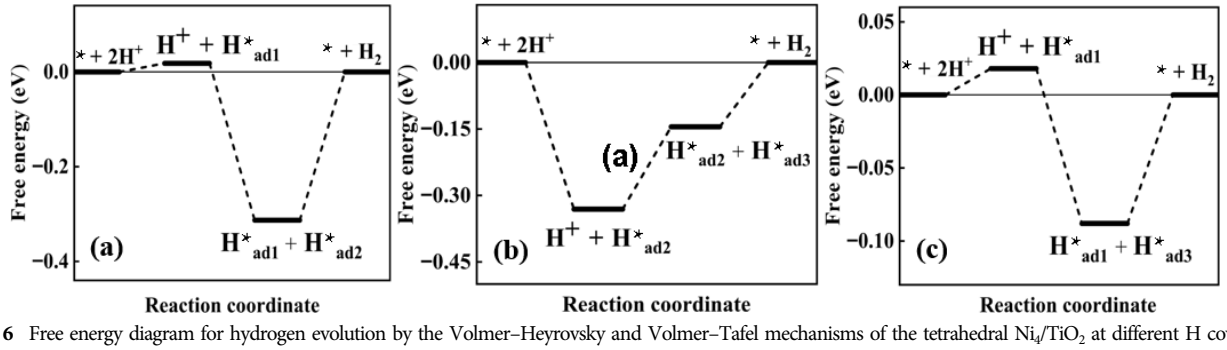

Figure 6 Free energy diagram for hydrogen evolution by the Volmer–Heyrovsky and Volmer–Tafel mechanisms of the tetrahedral Ni_4/TiO_2 at different H coverages under standard conditions (1 bar of H_2 and pH = 0 at 300 K) and the equilibrium potential U = 0. (a) 2H adsorption (2/3 monolayer) scenario, (b) and (c) 3H adsorption (1 monolayer) scenario respectively experienced the $H^*_{ad2} + H^*_{ad3}$ and $H^*_{ad1} + H^*_{ad3}$ combinations.

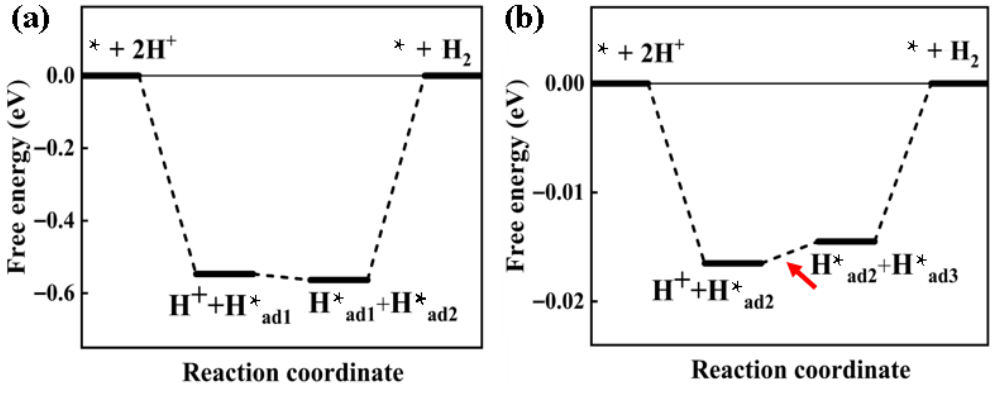

Figure 5 Free energy diagram for hydrogen evolution by the Volmer–Heyrovsky and Volmer–Tafel mechanisms of the planar rhombic Ni_4/TiO_2 at different H coverages under standard conditions (1 bar of H_2 and pH = 0 at 300 K) and the equilibrium potential U = 0. (a) 2H adsorption (2/3 monolayer) scenario and (b) 3H adsorption (1 monolayer) scenario.

Ni_{c1}–Ni_{c4} edge as a reactive species initiates and sustains the Volmer–Heyrovsky reaction, the catalyst exhibits good hydrogen production activity, with a ΔG_{H^*} of 0.02 eV. For H^*_{ad2} and H^*_{ad3}, the rate-determining steps are respectively the Heyrovsky reaction (with a ΔG_{H^*} of −0.33 eV) and the Volmer reaction (with a ΔG_{H^*} of 0.19 eV), as shown in Fig. 6(b). Furthermore, following the Volmer–Tafel mechanism, the H^*_{ad1} + H^*_{ad3} combination is able to proceed due to the ΔG_{H^*} of −0.09 eV (see Fig. 6(c)), which is almost comparable to that of Pd at 1 monolayer coverage of H [47]. The reaction is an endothermic process as before. Unfortunately, the ΔG_{H^*} for the H^*_{ad1} + H^*_{ad2} and H^*_{ad2} + H^*_{ad3} combinations for H_2 gas are −0.31 and −0.15 eV. The rate-determining steps are respectively the Tafel reaction and the Volmer reaction. Accordingly, we believe that the atomic utilization efficiency of the tetrahedral Ni_4/TiO_2 would be 1/4. From the perspective of available sites and reaction pathways, we can say that the atomic utilization efficiency and hydrogen production activity of the tetrahedral Ni_4/TiO_2 are far inferior to those of the planar rhombic Ni_4/TiO_2, highlighting the advantages and significance of FACs.

Based on previous results, we can identify the changes in hydrogen evolution activity and atomic utilization of TiO_2-supported Ni aggregates with increasing number of atoms from n = 1 to 4, as shown in Fig. 7. Note that to ensure comparability of the HER activity among numerous TiO_2-supported FACs, from a thermochemical perspective, we consider the Gibbs free energy of H adsorption (ΔG_{H^*}) for each elementary step of HER as a reference and a baseline benchmark for the development of efficient practical hydrogen production catalysts. Specific performance as follows: The Ni-SAC is a single-site catalyst, so the atomic utilization efficiency is 100%, but the hydrogen production activity (with a ΔG_{H^*} of −0.13 eV) is still lower that of Pt at 1/4 monolayer coverage of H (−0.10 eV) [32]; the Ni-DAC belongs to a dual-site catalyst due to the equal contribution of two metal centers, so the atomic utilization efficiency also reaches 100%, and the hydrogen production activity (with a ΔG_{H^*} of 0.03 eV) is close to that of Pt at 1 monolayer coverage of H (−0.03 eV) [33]; as for the Ni-TAC, although the Ni_3 trimer has the ability to capture three H atoms, only at θ_{H^*} = 2/3 monolayer H coverage, the H^*_{ad2} situated at the hollow site can initiate the hydrogen production reaction, following the Volmer–Heyrovsky mechanism. In that case, three metal atoms constitute an active site, so the atomic utilization efficiency is only 1/3, but the hydrogen production activity (with a ΔG_{H^*} of 0.05 eV) is slightly lower than Pt at 1 monolayer coverage of H [34]. Note

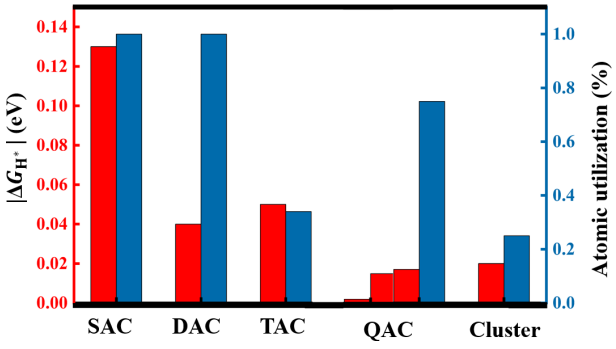

Figure 7 The hydrogen evolution activity ($|\Delta G_{H^*}|$) and atomic utilization of TiO_2-supported FACs containing Ni-SAC, DAC, TAC and QAC, and cluster catalyst (tetrahedral Ni_4/TiO_2). Red and blue columns represent the hydrogen evolution activity and atomic utilization of all catalysts, respectively. The reaction thermochemistry suggests that the smaller the $|\Delta G_{H^*}|$, the higher the activity of a catalyst towards HER, and vice versa.

that here the activity threshold of HER is based on the Gibbs free energy of H adsorption on Pt at full H coverage [47]. This is to ensure that the designed catalysts are excellent, that is, the hydrogen production process is near thermo-neutral (neither endothermic nor exothermic). Overall, we believe that Ni-DACs and Ni-QACs are the best choices for hydrogen production, despite their respective advantages in catalytic activity and atomic utilization. So fundamentally we can say that these variations in the structure–activity relationship and the synergistic effect are related to the coordination environment of the aggregate, specifically manifested as the confinement effect of the quantum well, which is formed by the metal aggregate surrounded by the surface O atoms of anatase TiO_2.

To make clear the reason that the TiO_2-supported Ni_4 tetramers have excellent HER activity, we perform a comprehensive electronic analysis by the calculation of DOS, charge transfer between Ni_4 and TiO_2, valence state distribution of metals, charge variation and localization/delocalization of metallic states on Ni_4 tetramers of two structurally different Ni_4/TiO_2 at different H coverages for an efficient hydrogen production process. The effect of the charge transfer between the metal aggregate and TiO_2 on the HER activity of Ni_4/TiO_2 can be assessed through the changes in the electronic valence state (or charge in Table S1 in the ESM) of metal atoms, so-called "overall reducibility" for the Ni aggregate. From Table S1 and Fig. S8(a) in the ESM, we see that except for hydroxylation occurred on the tetrahedral Ni_4/TiO_2, as the coverage of H increases in the reaction process, the total charge of Ni aggregates monotonically decreases, meaning the continuous reduction of protons from solution by combining with electrons at the Ni_4/TiO_2 electrode. More precisely, in the planar rhombic Ni_4/TiO_2, the order of active sites and the adsorption energy of H atoms in the reaction are consistent with the Bader charges and valence states/charge change of corresponding host Ni atoms (Table S1 in the ESM). Typically, the decreasing magnitude of the charge (Δq) for 1H adsorption scenario is larger than those for 2H and 3H adsorption scenarios (Fig. S8(a) in the ESM), proving that the H^*_{ad1} is independent of available sites. Meanwhile, the ratio of charge variation to total charge ($\Delta q/q$) on Ni_4 is as small as 0.1% (Fig. S8(b) in the ESM), indicative of a spatially delocalized state over the metal ensemble. A direct consequence is that the mutual influences of H^*_{ad1} and $H^*_{ad2,ad3}$ are very small in HER. This will allow the reduction-desorption processes of the latter two to be smooth, in line with their better HER performances. By contrast, in the tetrahedral Ni_4/TiO_2, the hydroxylation at the interface produces two unexpected results: (1) The decreasing magnitude of the charge (Δq) and associated ratio ($\Delta q/q$) at different H coverages are larger than those of the planar rhombic Ni_4/TiO_2 (Figs. S8(a) and S8(b) in the ESM); (2) in addition to the valence states of host Ni atoms (note that the active site is at the edge of the tetrahedra), the steric hindrance effect (from the edges and the interface) also simultaneously determines the HER activity and pathway (Figs. 4 and 6). The situation has become more complex and requires further specific research in the future.

More details about the reasons for different catalyst models with different HER activities can also be obtained from the DOS analysis, here mainly focusing on the commonalities and differences between different catalysts. For the two structurally different Ni_4/TiO_2, the commonalities are that the Ni-d states are inside the band gap of TiO_2, and are delocalized over the entire Ni_4 tetramer, manifested as local metallic states, and meanwhile, the tail of the Ni-

d states hybrids with the O_{2c}-p states at the valence band maximum about 2.2–2.5 below the Fermi level for the planar rhombic Ni_4/TiO_2 (Figs. S2 and S3 in the ESM) and 2.8–3.5 eV below the Fermi level for the tetrahedral Ni_4/TiO_2 (Figs. S5 and S6 in the ESM). This indicates that the coordination environment of the Ni_4 tetramer is only of surface oxygen atoms and the quantum confinement is achieved through p-d hybridization, which creates a potential well to confine the metallic states of Ni_4. The differences are that a large amount of electronic states that are primarily derived from the d orbitals of $Ni_{c1,c2,c4}$ and the s orbitals of $H^*_{ad1,ad2}$ appear at the Fermi level for the tetrahedral structure (see Figs. S5 and S7 in the ESM), whereas no electronic states appear at the Fermi level for the planar rhombic structure (see Figs. S2 and S4 in the ESM). This means that the tetrahedral Ni_4/TiO_2, similar to bulk Ni, have strong H binding gained from s-d hybridization, which is not conducive to hydrogen production. There are three Ni atoms that contribute to strong H-binding, thereby substantially reducing the atomic utilization of the tetrahedral Ni_4/TiO_2. By comparison, the planar rhombic Ni_4/TiO_2 will supply electrons to protons from solution to form first H atoms on the Ni_4 tetramer and then H_2 molecules through the occupied states below the Fermi level, which are mainly from the Ni-d orbitals with a small amount of $H^*_{ad2,ad3}$-s orbitals at the energy range from −0.80 to −2.30 eV (see Fig. S4 in the ESM). Relatively, the states originated from the H^*_{ad1} adsorption are basically assigned at the lower energy region (about −4.10 eV), indicative of a stronger H-binding to Ni_4 than those of $H^*_{ad2,ad3}$ scenarios. Overall, smaller H-binding provided by a large number of Ni atoms of the tetramer, which is consistent with the d-band center further away from the Fermi level, allows for better HER activity and higher atomic utilization efficiency of the planar rhombic Ni_4/TiO_2 than the tetrahedral Ni_4/TiO_2.

Our DFT calculations are based on the constant charge model (CCM) for the ground states of TiO_2-supported FACs. Strictly speaking, we should perform a constant potential model (CPM) calculation by using grand canonical DFT to describe the electrochemical reactions. Typically, Tan et al. investigated the HER behaviors of SA TM–N_xC_y motifs and proposed that the quantitative difference of ΔG_{H^*} between the CCM and CPM is proportional in some way to the total charge change before and after H adsorption, due to the change of electronic occupation states [68]. Specifically for this series of studies on TiO_2-supported FACs, considering the strict threshold for the HER activity (comparable to that of Pt), we believe that HER on available FACs is thermo-neutral at the equilibrium potential. At this rate, there is no need to consider increasing the applied potential U (≈ 0) to break the equilibrium, preventing hydrogen production efficiency. From Table S1 and Fig. S2 in the ESM, we see that during the HER process, the total charge change and the electronic occupation states of the Ni_4 tetramer is relatively small and remain unchanged before and after H adsorption, indicating that the charge effect on the HER activity of the planar rhombic Ni_4/TiO_2 is insignificant, and the deviation of the Fermi level can be ignored. All in all, these results indicate that TiO_2-supported Ni-FACs exhibit relatively small calculation errors between the CCM and CPM. We believe the reason is that local metallic states delocalized over the entire Ni_4 tetramer that provides active sites make it insensitive to the charge effect induced by H adsorption in practical electrochemical reactions. To some extent, it is feasible to use the CCM to approximately replace the CPM in calculating the Gibbs free energy of H adsorption for assessing the HER activity. From a semi-quantitative perspective, the results and conclusions from the CCM are credible and meaningful. More importantly, our electronic structure analysis satisfies the classical d-band center theory (see Figs. S2 and S4 in the ESM vs. Figs. S5 and S7 in the ESM). Of course, in order to achieve perfection, this point about the HER activity dependence on the charge effect deserves further comments by using CPM calculations.

According to the growth habit, property-related structural characteristics and structure-dependent catalytic performance for hydrogen production of Ni_4/TiO_2, at the atomic level, we now introduce the definitions and differences between FACs and cluster catalysts. For oxide-supported FACs, each central metal atom in a close-packed arrangement coordinates with the O atom of the support, forming an "atomic interface" [46], and then exhibits a moderate oxidation state (+δ) by the "point-to-point" local electron transfer. Simply put, each metal atom has a similar coordination environment, which determines the performance of the catalyst. The aggregate can be functioned as an enlarged metal-like pseudo-atom with locally indistinguishable quantum states and multiple active sites. Thereinto, multiple active sites composed of all precisely arranged metal centres have diversity and variability, but providing the highest possible atomic utilization efficiency. The typical examples are the planar rhombic Ni_4/TiO_2, TACs [14, 15] and DACs [11–13]. By contrary, in atomically dispersed cluster catalysts there are at least two kinds of metal atoms with totally different valence states, which are attributable to the different coordination environments. The oxidation state (+δ) of most central metal atoms is realized by the "point-to-bulk" interfacial electron transfer [69]. Since there are always some constituent atoms that are not the active sites, the atomic utilization efficiency is lower. Representative examples include the tetrahedral Ni_4/TiO_2 and fully exposed cluster catalysts [27–29]. On the whole, this once again indicates the turning point between FACs and cluster catalysts, which can be distinguished by the coordination environment of central metal atoms and structure-dependent catalytic performance of the catalysts for high atomic utilization. The classification is based on the idea of SACs. From the perspective of the number of metal atoms in the active center, FACs is a bridge connecting SACs and cluster or nanoparticle catalysts.

4 Conclusions

We use the number of metal atoms instead of the size of aggregates as the independent variable to study the structure and catalytic performance of TiO_2-supported FACs, aiming to identify the atomic utilization efficiency. According to the growth habit, property-related structural characteristics and structure-dependent catalytic performance for hydrogen production, we systematize the definitions and differences between FACs and atomically dispersed cluster catalysts. Simply put, each central atom of the aggregate for FACs is coordinated to the support, and exhibits locally indistinguishable quantum states and a moderate oxidation state, allowing for multiple active sites for one-step and multi-step reactions and achieving high atomic utilization and reaction activity simultaneously. By leveraging the electronic and geometric advantages, the planar rhombic and tetrahedral Ni_4 tetramers can nucleate and grow on anatase TiO_2 (101) surfaces under the suitable operating conditions. The two structurally different Ni_4/TiO_2, respectively belonging to FACs and cluster catalysts, have quite different metal valence state distributions and binding modes. The point is, the planar rhombic Ni_4/TiO_2 yields an atomic utilization efficiency of 75%, somewhat close to that of SACs, and

better hydrogen production activity than SACs. In the TiO_2-supported ADMCs family, Ni_4/TiO_2 is a crucial point that distinguishes FACs from cluster catalysts. This phenomenon is expected to be applicable to all oxide-supported metal catalysts. We are confident that FACs will bridge between SACs and cluster or nanoparticle catalysts, and the design strategy and principles described can be generalized to most FACs with high atomic utilization and reaction activity, especially for multi-step reactions.

Electronic Supplementary Material: Supplementary material (Figs. S1–S8 and Table S1) is available in the online version of this article at https://doi.org/10.26599/NR.2025.94907293.

Data availability

All data needed to support the conclusions in the paper are presented in the manuscript and the Electronic Supplementary Material. Additional data related to this paper may be requested from the corresponding author upon request.

Acknowledgements

This work was supported by the National Natural Science Foundation of China (No. 52272199).

Declaration of competing interest

All the contributing authors report no conflict of interests in this work.

Author contribution statement

F. R. C.: Data curation, project administration, writing manuscript. G. C. Z.: Validation. G. Z.: Project administration, funding acquisition, writing manuscript. All the authors have approved the final manuscript.

Use of AI statement

None.

References

[1] Yang, X. F.; Wang, A. Q.; Qiao, B. T.; Li, J.; Liu, J. Y.; Zhang, T. Single-atom catalysts: A new frontier in heterogeneous catalysis. *Acc. Chem. Res.* **2013**, *46*, 1740–1748.

[2] Zhang, H. B.; Liu, G. G.; Shi, L.; Ye, J. H. Single-atom catalysts: Emerging multifunctional materials in heterogeneous catalysis. *Adv. Energy Mater.* **2018**, *8*, 1701343.

[3] Zhuang, Z. C.; Kang, Q.; Wang, D. S.; Li, Y. D. Single-atom catalysis enables long-life, high-energy lithium-sulfur batteries. *Nano Res.* **2020**, *13*, 1856–1866.

[4] Du, Y. X.; Sheng, H. T.; Astruc, D.; Zhu, M. Z. Atomically precise noble metal nanoclusters as efficient catalysts: A bridge between structure and properties. *Chem. Rev.* **2020**, *120*, 526–622.

[5] Zheng, X. B.; Li, B. B.; Wang, Q. S.; Wang, D. S.; Li, Y. D. Emerging low-nuclearity supported metal catalysts with atomic level precision for efficient heterogeneous catalysis. *Nano Res.* **2022**, *15*, 7806–7839.

[6] Li, R. Z.; Wang, D. S. Understanding the structure–performance relationship of active sites at atomic scale. *Nano Res.* **2022**, *15*, 6888–6923.

[7] Qiao, B. T.; Wang, A. Q.; Yang, X. F.; Allard, L. F.; Jiang, Z.; Cui, Y. T.; Liu, J. Y.; Li, J.; Zhang, T. Single-atom catalysis of CO oxidation using Pt_1/FeO_x. *Nat. Chem.* **2011**, *3*, 634–641.

[8] Liu, L. C.; Corma, A. Metal catalysts for heterogeneous catalysis: From single atoms to nanoclusters and nanoparticles. *Chem. Rev.* **2018**, *118*, 4981–5079.

[9] Lu, X. W.; Guo, C. M.; Zhang, M. Y.; Leng, L. P.; Horton, J. H.; Wu, W.; Li, Z. J. Rational design of palladium single-atoms and clusters supported on silicoaluminophosphate-31 by a photochemical route for chemoselective hydrodeoxygenation of vanillin. *Nano Res.* **2021**, *14*, 4347–4355.

[10] Wang, Y.; Zheng, X. B.; Wang, D. S. Design concept for electrocatalysts. *Nano Res.* **2022**, *15*, 1730–1752.

[11] Ying, Y. R.; Luo, X.; Qiao, J. L.; Huang, H. T. "More is different": Synergistic effect and structural engineering in double-atom catalysts. *Adv. Funct. Mater.* **2021**, *31*, 2007423.

[12] Yan, Y.; Cheng, H. Y.; Qu, Z. H.; Yu, R.; Liu, F.; Ma, Q. W.; Zhao, S.; Hu, H.; Cheng, Y.; Yang, C. Y. et al. Recent progress on the synthesis and oxygen reduction applications of Fe-based single-atom and double-atom catalysts. *J. Mater. Chem. A* **2021**, *9*, 19489–19507.

[13] Wang, Y. N.; Wan, X.; Liu, J. Y.; Li, W. W.; Li, Y. C.; Guo, X.; Liu, X. F.; Shang, J. X.; Shui, J. L. Catalysis stability enhancement of Fe/Co dual-atom site via phosphorus coordination for proton exchange membrane fuel cell. *Nano Res.* **2022**, *15*, 3082–3089.

[14] Chen, Z. W.; Chen, L. X.; Yang, C. C.; Jiang, Q. Atomic (single, double, and triple atoms) catalysis: Frontiers, opportunities, and challenges. *J. Mater. Chem. A* **2019**, *7*, 3492–3515.

[15] Hou, C. C.; Wang, H. F.; Li, C. X.; Xu, Q. From metal-organic frameworks to single/dual-atom and cluster metal catalysts for energy applications. *Energy Environ. Sci.* **2020**, *13*, 1658–1693.

[16] Chen, Y.; Lin, J.; Jia, B. H.; Wang, X. D.; Jiang, S. Y.; Ma, T. Y. Isolating single and few atoms for enhanced catalysis. *Adv. Mater.* **2022**, *34*, 2201796.

[17] Li, X. Y.; Rong, H. P.; Zhang, J. T.; Wang, D. S.; Li, Y. D. Modulating the local coordination environment of single-atom catalysts for enhanced catalytic performance. *Nano Res.* **2020**, *13*, 1842–1855.

[18] Zhang, J. C.; Yang, H. B.; Liu, B. Coordination engineering of single-atom catalysts for the oxygen reduction reaction: A review. *Adv. Energy Mater.* **2021**, *11*, 2002473.

[19] Chen, Z. W.; Yan, J. M.; Jiang, Q. Single or double: Which is the altar of atomic catalysts for nitrogen reduction reaction. *Small Methods* **2019**, *3*, 1800291.

[20] Liu, J. C.; Ma, X. L.; Li, Y.; Wang, Y. G.; Xiao, H.; Li, J. Heterogeneous Fe_3 single-cluster catalyst for ammonia synthesis via an associative mechanism. *Nat. Commun.* **2018**, *9*, 1610.

[21] Gan, T.; Wang, D. S. Atomically dispersed materials: Ideal catalysts in atomic era. *Nano Res.* **2024**, *17*, 18–38.

[22] Yan, H.; Lin, Y.; Wu, H.; Zhang, W. H.; Sun, Z. H.; Cheng, H.; Liu, W.; Wang, C. L.; Li, J. J.; Huang, X. H. et al. Bottom-up precise synthesis of stable platinum dimers on graphene. *Nat. Commun.* **2017**, *8*, 1070.

[23] Tian, S. B.; Fu, Q.; Chen, W. X.; Feng, Q. C.; Chen, Z.; Zhang, J.; Cheong, W. C.; Yu, R.; Gu, L.; Dong, J. C. et al. Carbon nitride supported Fe_2 cluster catalysts with superior performance for alkene epoxidation. *Nat. Commun.* **2018**, *9*, 2353.

[24] Lei, Y.; Mehmood, F.; Lee, S.; Greeley, J.; Lee, B.; Seifert, S.; Winans, R. E.; Elam, J. W.; Meyer, R. J.; Redfern, P. C. et al. Increased silver activity for direct propylene epoxidation via subnanometer size effects. *Science* **2010**, *328*, 224–228.

[25] Ji, S. F.; Chen, Y. J.; Fu, Q.; Chen, Y. F.; Dong, J. C.; Chen, W. X.; Li, Z.; Wang, Y.; Gu, L.; He, W. et al. Confined pyrolysis within metal-organic frameworks to form uniform Ru_3 clusters for efficient oxidation of alcohols. *J. Am. Chem. Soc.* **2017**, *139*, 9795–9798.

[26] Liu, C. Y.; Tan, Y. Z.; Lin, S. S.; Li, H.; Wu, X. J.; Li, L.; Pei, Y.; Zeng, X. C. CO self-promoting oxidation on nanosized gold clusters: Triangular Au_3 active site and CO induced O–O scission. *J. Am. Chem. Soc.* **2013**, *135*, 2583–2595.

[27] Zhang, J. Y.; Deng, Y. C.; Cai, X. B.; Chen, Y. L.; Peng, M.; Jia, Z. M.; Jiang, Z.; Ren, P. J.; Yao, S. Y.; Xie, J. L. et al. Tin-assisted fully exposed platinum clusters stabilized on defect-rich graphene for dehydrogenation reaction. *ACS Catal.* **2019**, *9*, 5998–6005.

[28] Jeong, H.; Lee, G.; Kim, B. S.; Bae, J.; Han, J. W.; Lee, H. Fully dispersed Rh ensemble catalyst to enhance low-temperature activity. *J. Am. Chem. Soc.* **2018**, *140*, 9558–9565.

[29] Peng, M.; Dong, C. Y.; Gao, R.; Xiao, D. Q.; Liu, H. Y.; Ma, D. Fully exposed cluster catalyst (FECC): Toward rich surface sites and full atom utilization efficiency. *ACS Cent. Sci.* **2021**, *7*, 262–273.

[30] Chen, W. T.; Chan, A.; Sun-Waterhouse, D.; Moriga, T.; Idriss, H.; Waterhouse, G. I. N. Ni/TiO_2: A promising low-cost photocatalytic system for solar H_2 production from ethanol-water mixtures. *J. Catal.* **2015**, *326*, 43–53.

[31] Eder, M.; Courtois, C.; Kratky, T.; Günther, S.; Tschurl, M.; Heiz, U. Nickel clusters on TiO_2(110): Thermal chemistry and photocatalytic hydrogen evolution of methanol. *Catal. Sci. Technol.* **2020**, *10*, 7630–7639.

[32] Bi, H.; Zhang, L.; Wang, Z. Y.; Zhou, G. Identification of active sites available for hydrogen evolution of single-atom Ni_1/TiO_2 catalysts. *Appl. Surf. Sci.* **2022**, *579*, 152139.

[33] Liu, J. L.; Bi, H.; Zhang, L.; Zhou, G. Transition metal dual-atom Ni_2/TiO_2 catalysts for photoelectrocatalytic hydrogen evolution: A density functional theory study. *Appl. Surf. Sci.* **2023**, *608*, 155132.

[34] Liu, J. L.; Wang, Z. H.; Chen, F. R.; Zhou, G. Self-assembly, structure and catalytic activity of Ni_3 on TiO_2: A triple-atom catalyst for hydrogen evolution. *Appl. Surf. Sci.* **2024**, *643*, 158719.

[35] Choi, W.; Termin, A.; Hoffmann, M. R. The role of metal ion dopants in quantum-sized TiO_2: Correlation between photoreactivity and charge carrier recombination dynamics. *J. Phys. Chem.* **1994**, *98*, 13669–13679.

[36] Low, J.; Cheng, B.; Yu, J. G. Surface modification and enhanced photocatalytic CO_2 reduction performance of TiO_2: A review. *Appl. Surf. Sci.* **2017**, *392*, 658–686.

[37] Kresse, G.; Furthmüller, J. Efficiency of *ab-initio* total energy calculations for metals and semiconductors using a plane-wave basis set. *Comput. Mater. Sci.* **1996**, *6*, 15–50.

[38] Kresse, G.; Furthmüller, J. Efficient iterative schemes for *ab initio* total-energy calculations using a plane-wave basis set. *Phys. Rev. B* **1996**, *54*, 11169–11186.

[39] Hammer, B.; Hansen, L. B.; Nørskov, J. K. Improved adsorption energetics within density-functional theory using revised perdew–burke–ernzerhof functionals. *Phys. Rev. B* **1999**, *59*, 7413–7421.

[40] Blöchl, P. E. Projector augmented-wave method. *Phys. Rev. B* **1994**, *50*, 17953–17979.

[41] Anisimov, V. I.; Zaanen, J.; Andersen, O. K. Band theory and Mott insulators: Hubbard *U* instead of stoner *I*. *Phys. Rev. B* **1991**, *44*, 943–954.

[42] Anisimov, V. I.; Aryasetiawan, F.; Lichtenstein, A. I. First-principles calculations of the electronic structure and spectra of strongly correlated systems: The LDA + *U* method. *J. Phys. Condens. Matter* **1997**, *9*, 767–808.

[43] Burdett, J. K.; Hughbanks, T.; Miller, G. J.; Richardson, J. W. Jr. ; Smith, J. V. Structural–electronic relationships in inorganic solids: Powder neutron diffraction studies of the rutile and anatase polymorphs of titanium dioxide at 15 and 295 K. *J. Am. Chem. Soc.* **1987**, *109*, 3639–3646.

[44] Monkhorst, H. J.; Pack, J. D. Special points for Brillouin-zone integrations. *Phys. Rev. B* **1976**, *13*, 5188–5192.

[45] Xing, J.; Chen, J. F.; Li, Y. H.; Yuan, W. T.; Zhou, Y.; Zheng, L. R.; Wang, H. F.; Hu, P.; Wang, Y.; Zhao, H. J. et al. Stable isolated metal atoms as active sites for photocatalytic hydrogen evolution. *Chem. - Eur. J.* **2014**, *20*, 2138–2144.

[46] Chen, Y. J.; Ji, S. F.; Sun, W. M.; Lei, Y. P.; Wang, Q. C.; Li, A.; Chen, W. X.; Zhou, G.; Zhang, Z. D.; Wang, Y. et al. Engineering the atomic interface with single platinum atoms for enhanced photocatalytic hydrogen production. *Angew. Chem., Int. Ed.* **2020**, *59*, 1295–1301.

[47] Nørskov, J. K.; Bligaard, T.; Logadottir, A.; Kitchin, J. R.; Chen, J. G.; Pandelov, S.; Stimming, U. Trends in the exchange current for hydrogen evolution. *J. Electrochem. Soc.* **2005**, *152*, J23–J26.

[48] Hinnemann, B.; Moses, P. G.; Bonde, J.; Jørgensen, K. P.; Nielsen, J. H.; Horch, S.; Chorkendorff, I.; Nørskov, J. K. Biomimetic hydrogen evolution: MoS_2 nanoparticles as catalyst for hydrogen evolution. *J. Am. Chem. Soc.* **2005**, *127*, 5308–5309.

[49] Peterson, A. A.; Abild-Pedersen, F.; Studt, F.; Rossmeisl, J.; Nørskov, J. K. How copper catalyzes the electroreduction of carbon dioxide into hydrocarbon fuels. *Energy Environ. Sci.* **2010**, *3*, 1311–1315.

[50] Fujikawa, K.; Suzuki, S.; Koike, Y.; Chun, W. J.; Asakura, K. Self-regulated Ni cluster formation on the TiO_2(110) terrace studied using scanning tunneling microscopy. *Surf. Sci.* **2006**, *600*, 117–121.

[51] Mahesh, K. P. O.; Kuo, D. H. Synthesis of Ni nanoparticles decorated SiO_2/TiO_2 magnetic spheres for enhanced photocatalytic activity towards the degradation of azo dye. *Appl. Surf. Sci.* **2015**, *357*, 433–438.

[52] Wang, Y. X.; Cui, X. Z.; Zhang, J. Q.; Qiao, J. L.; Huang, H. T.; Shi, J. L.; Wang, G. X. Advances of atomically dispersed catalysts from single-atom to clusters in energy storage and conversion applications. *Prog. Mater. Sci.* **2022**, *128*, 100964.

[53] Dong, F.; Wu, M. J.; Chen, Z. S.; Liu, X. H.; Zhang, G. X.; Qiao, J. L.; Sun, S. H. Atomically dispersed transition metal-nitrogen-carbon bifunctional oxygen electrocatalysts for zinc-air batteries: Recent advances and future perspectives. *Nano-Micro Lett.* **2022**, *14*, 36.

[54] Hashem, A.; Hossain, M. A. M.; Marlinda, A. R.; Mamun, M. A.; Simarani, K.; Johan, M. R. Nanomaterials based electrochemical nucleic acid biosensors for environmental monitoring: A review. *Appl. Surf. Sci. Adv.* **2021**, *4*, 100064.

[55] Shen, Q.; Gao, H. Y.; Fuchs, H. Frontiers of on-surface synthesis: From principles to applications. *Nano Today* **2017**, *13*, 77–96.

[56] Zhang, L.; Bi, H.; Wang, Z. Y.; Zhou, G. Insight into enhanced hydrogen evolution of single-atom Cu_1/TiO_2 catalysts from first principles. *Int. J. Hydrogen Energy* **2022**, *47*, 4653–4661.

[57] Jin, C.; Dai, Y.; Wei, W.; Ma, X. C.; Li, M. M.; Huang, B. B. Effects of single metal atom (Pt, Pd, Rh and Ru) adsorption on the photocatalytic properties of anatase TiO_2. *Appl. Surf. Sci.* **2017**, *426*, 639–646.

[58] Yang, K.; Zhou, G. Hydrogen evolution/spillover effect of single cobalt atom on anatase TiO_2 from first-principles calculations. *Appl. Surf. Sci.* **2021**, *536*, 147831.

[59] Experimental data referred from the Materials Studio Structures Library.

[60] Venables, J. A.; Spiller, G. D. T.; Hanbucken, M. Nucleation and growth of thin films. *Rep. Prog. Phys.* **1984**, *47*, 399–459.

[61] Campbell, C. T. Ultrathin metal films and particles on oxide surfaces: Structural, electronic and chemisorptive properties. *Surf. Sci. Rep.* **1997**, *27*, 1–111.

[62] Wang, Z. H.; Tang, W.; Liu, J. L.; Zhou, G. An interesting synergistic effect of heteronuclear dual-atom catalysts for hydrogen production: Offsetting or promoting. *Nano Res.* **2024**, *17*, 5742–5752.

[63] Guo, Y. L.; Wen, M. C.; Li, G. Y.; An, T. C. Recent advances in VOC elimination by catalytic oxidation technology onto various nanoparticles catalysts: A critical review. *Appl. Catal. B: Environ.* **2021**, *281*, 119447.

[64] Li, Z.; Ji, S. F.; Liu, Y. W.; Cao, X.; Tian, S. B.; Chen, Y. J.; Niu, Z. Q.; Li, Y. D. Well-defined materials for heterogeneous catalysis: From nanoparticles to isolated single-atom sites. *Chem. Rev.* **2020**, *120*, 623–682.

[65] Van Deelen, T. W.; Mejia, C. H.; De Jong, K. P. Control of metal-support interactions in heterogeneous catalysts to enhance activity and selectivity. *Nat. Catal.* **2019**, *2*, 955–970.

[66] Vayssilov, G. N.; Lykhach, Y.; Migani, A.; Staudt, T.; Petrova, G. P.; Tsud, N.; Skála, T.; Bruix, A.; Illas, F.; Prince, K. C. et al. Support nanostructure boosts oxygen transfer to catalytically active platinum nanoparticles. *Nat. Mater.* **2011**, *10*, 310–315.

[67] Bockris, J. O.; Reddy, A. K. N. *Modern Electrochemistry: An Introduction to an Interdisciplinary Area*; Springer: New York, 1970.

[68] Tan, S. Y.; Ji, Y. J.; Li, Y. Y. Single-atom electrocatalysis for hydrogen evolution based on the constant charge and constant potential models. *J. Phys. Chem. Lett.* **2022**, *13*, 7036–7042.

[69] Yao, S. Y.; Zhang, X.; Zhou, W.; Gao, R.; Xu, W. Q.; Ye, Y. F.; Lin, L. L.; Wen, X. D.; Liu, P.; Chen, B. B. et al. Atomic-layered Au clusters on α-MoC as catalysts for the low-temperature water-gas shift reaction. *Science* **2017**, *357*, 389–393.